nature communications

Article

https://doi.org/10.1038/s41467-025-58871-7

Probing nuclear quantum effects in electrocatalysis via a machine-learning enhanced grand canonical constant potential approach

Received: 6 September 2024

Accepted: 2 April 2025

Published online: 16 April 2025

Check for updates

Menglin Sun[1,4], Bin Jin[1,4], Xiaolong Yang[1,4] & Shenzhen Xu[1,2,3]

Proton-coupled electron transfer (PCET) is the key step for energy conversion in electrocatalysis. Atomic-scale simulation acts as an indispensable tool to provide a microscopic understanding of PCET. However, consideration of the quantum nature of transferring protons under an exact grand canonical constant potential condition is a great challenge for theoretical electrocatalysis. Here, we develop a unified computational framework to explicitly treat nuclear quantum effects (NQEs) by a sufficient grand canonical sampling, further assisted by a machine learning force field adapted for electrochemical conditions. Our work demonstrates a non-negligible impact of NQEs on PCET simulations for hydrogen evolution reaction at room temperature, and provides a physical picture that wave-like quantum characteristic of the transferring protons facilitates the particles to tunnel through classical barriers in PCET paths, leading to a remarkable activation energy reduction compared to classical simulations. Moreover, the physical insight of NQEs may reshape our fundamental understanding of other types of PCET reactions in broader scenarios of energy conversion processes.

Understanding and controlling energy conversion processes are the key to the development of innovative green energy technologies. Electrochemical catalysis on various electrode materials facilitates efficient conversion between transient electrical energies and stable chemical energies, for example, electrocatalytic hydrogen evolution reactions (HER)[1] during water splitting, oxygen reduction reactions (ORR)[2] in fuel cells, electrochemical CO_2 reduction reactions (CO_2RR)[3] which simultaneously mitigates CO_2 emission and produces fuels. Proton-coupled electron transfer (PCET), an essential elementary reaction step shared by most of the electrochemical energy conversion systems, determines the reaction rates, efficiencies, and selectivity of different electrocatalytic cells. Deep insights and understanding of the proton transfer step in complex environment near the electrode/solvent interfaces thus draw great attention and interests from the community of electrochemistry and chemical physics.

For a typical PCET process in electrochemical systems of metal/aqueous solution interfaces, a proton originally from the H_2O network transfers toward catalytic metal sites or a certain reactant species, accompanied by electron transfer (via electrode surfaces) under a constant potential condition. Detecting and observing these intricate and localized events at a microscopic level presents a challenge for experimental methods, across both spatial and temporal dimensions. However, atomic simulations offer a powerful alternative, allowing us to examine the kinetics and thermodynamics of elementary PCET steps. From the above conceptual description of PCET, we can obtain three key requirements that would be critical in theoretical modeling:

[1]School of Materials Science and Engineering, Peking University, Beijing, People's Republic of China. [2]AI for Science Institute, Beijing, People's Republic of China. [3]Beijing Key Laboratory of Theory and Technology for Advanced Battery Materials, School of Materials Science and Engineering, Peking University, Beijing, People's Republic of China. [4]These authors contributed equally: Menglin Sun, Bin Jin, Xiaolong Yang. e-mail: xushenzhen@pku.edu.cn

(1) a sufficient sampling of complex electrode/solvent interfacial environment; (2) a constant potential condition corresponding to a grand canonical (GC) ensemble; (3) a physically appropriate and exact treatment for protons involved in a PCET process.

Electrochemical theorists have developed many different approaches for modeling PCET reactions in the past decades. One of the most widely used methods is the computational hydrogen electrode (CHE) model[4] originally proposed by Nørskov and colleagues, by which the thermodynamic reaction energies under a certain applied potential can be computed, referred to as the standard hydrogen electrode (SHE) or the reversible hydrogen electrode (RHE). Extension to kinetic barrier calculations considering a constant potential condition was achieved in 2016[5,6]. The charge extrapolation method adjusts potential energy surfaces (PES) that are initially calculated with a constant charge model. This adjustment accounts for the electric double layer (EDL) at electrode/solvent interfaces, using a capacitor model to approximate the *a posteriori* correction terms. The great advantages of low computational cost and easy implementation make the above approaches popular in the electrochemistry community of PCET simulations. However, it is widely acknowledged that there are shortcomings in the approach, which considers only the initial states (IS), final states (FS), and transition states (TS) along a specific single path of the PCET steps, leading to a lack of configurational sampling. The charge extrapolation method, although applying a constant potential correction term, is not an exact treatment for the constant potential GC ensemble, one issue is that the TS is actually optimized under a constant charge model.

Regarding the necessity of sufficient configurational sampling involving electrode surface, reactant species, and solvent (usually H_2O) environment, several groups employed first-principles constrained molecular dynamics (CMD)[7,8] to calculate mean forces (or free energy gradients) at different reaction coordinates (RC) along a reaction path[9–11], in which the RC is predefined to describe reactions' progress. Configurational sampling is indeed performed by this method, while the expensive ab initio calculations limit the total MD steps along a trajectory (only ~10^4 steps), the sufficiency of statistical sampling thus is still questionable. This limitation actually could be addressed by the employment of machine learning potentials (MLPs), which will be presented and discussed in this work. CMD itself cannot provide a constant potential GC ensemble condition, two strategies were employed by previous studies, one is adding *a posteriori* constant potential correction term derived from the charge extrapolation scheme[12], and the other strategy is using the so-called grand canonical density functional theory (GC-DFT) method[13,14], in which the Fermi level referred to the vacuum level (or the work function) is fixed at a certain value. This can be accomplished by iteratively varying the system's total number of electrons in self-consistent field (SCF) loops until the system's work function is converged to the targeted value. On the basis of the GC-DFT and ab-initio-based CMD method, Liu group achieved a constant-potential condition by updating N_e every few MD steps based on a constant-capacitance assumption[15,16]. Further developments of the GC-DFT method were also reported recently to achieve more efficient convergence of targeted potentials[17,18]. However, fixing the work function of each sampled configuration actually does not resemble the microstates' distribution corresponding to an exact GC ensemble, which will be discussed later in this work. Moreover, this GC-DFT approach could induce an issue when dealing with quantized protons under a GC ensemble when the system's total electron number is allowed to vary, please refer to Supplementary Note 1 for detailed discussion.

Proton is the key transferring species in PCET reactions. Since hydrogen is the lightest element in nature, it is well known that the nuclear quantum effects (NQEs) dominate the mechanism of proton transfers at extremely low temperatures. Most of the previous theoretical work on PCET steps in electrochemical catalysis did not consider NQEs, partially due to the relatively high temperature of a standard condition (~ 300 K) and the expensive computational cost required. However, a bunch of earlier studies have revealed that the quantum nature of protons plays an important role at room temperature in proton transfer processes in liquid water[19], small organic molecules[20,21], biological macro molecules[22], and even crystalline oxide materials[23]. It is, therefore, inspiring to raise a question about the impact of NQEs in PCET steps of electrocatalysis. Hammes-Schiffer group pioneered the investigation on the quantum effect of homogeneous and heterogeneous PCET[24]. The computational method developed by the group provides a Fermi golden rule expression[25] of PCET reaction rates, in which vibronic states (the direct product of electronic states and proton vibrational states) are employed to compute the vibronic coupling term[26]. Both of the nonadiabatic effect and NQEs can be incorporated under this theoretical framework. The fundamental principle of this method is exact; however, certain limitations might exist when we numerically obtain the requested parameters for a realistic system or reaction process. For example, sufficient configurational sampling of the electrochemical environment at the electrode/solvent interface is lacking. Moreover, the approximated quantum treatment of protons in PCET, in which 1-D wavefunctions are solved along the oxidized and reduced diabatic PES of proton transfers[24], is not fully exact to compute the vibronic coupling term. An analogous framework for addressing nuclear tunneling and non-adiabaticity under electrochemical conditions was proposed by Melander, showing how we could compute electrochemical rate under a Marcus theory-type framework in a grand canonical ensemble condition[27]. However, Melander currently just considered an adiabatic classical model for the acidic Volmer reaction when applying the method in this recent paper[27], ignoring NQEs and non-adiabaticity (incorporation of which could still be on-going). As suggested by the Hammes-Schiffer group[24] and well acknowledged by the quantum dynamics community, the Feynman path integral (PI) algorithm[28,29] is a more exact simulation approach for proton quantization, which will be employed in this work.

Our goal is to investigate the NQEs of PCET under a constant potential electrochemical condition, which can be conducted by a unified statistical sampling framework developed by this study. We employ a grand canonical hybrid Monte Carlo (GC-HMC) algorithm to equilibrate the system with an external electronic reservoir at a certain chemical potential of electrons and combine with a path integral Monte Carlo (PIMC) method to take account of NQEs. We also develop an MLP adapted for electrochemical simulations on the basis of the Deep Potential (DP)[30], in which the total electron number of the interface system can be adjusted to realize a GC sampling, and we refer to this MLP as DP-N_e throughout this paper. This DP-N_e MLP significantly improves computational efficiency while maintaining a DFT level accuracy, enabling sufficient statistical sampling in our work with an affordable computational cost.

Electrocatalytic HER is a notable green-energy technology producing clean fuels[31], it consists of multiple possible PCET steps, which is an ideal modeling system in electrochemistry. We thus are interested in the NQEs on the thermodynamics and kinetics of elementary PCET steps of HER in this study. The Volmer step ($H^+_{sol} + e^- + * \rightarrow H^*$, where H^+_{sol} represents a solvated proton in water solution, e^- comes from a cathode, and "*" means a surface site at cathode surface) and the Heyrovsky step ($H^+_{sol} + e^- + H^* \rightarrow H_2$) are the two fundamental PCET steps, with another non-electrochemical Tafel step ($H^* + H^* \rightarrow H_2$) being investigated in this work as well (Supplementary Note 10). Researchers have done extensive theoretical studies on PCET steps in HER, typically by employing the CHE model and the charge extrapolation scheme[32–34]. The exact mechanism and quantitative kinetic properties of the above PCET steps are still under debate, with discrepancies of activation energies between the computational predictions and experimental results[35–38]. A recent theoretical work using the CMD method tried to reconcile the above-mentioned discrepancies[12], but there are still unresolved issues about the competitive relationship between the Volmer-Tafel and Volmer-Heyrovsky mechanisms.

With the NQEs being explicitly considered in this study, we attempt to provide new insights into the impact of this quantum effect on the PCET steps involved in electrocatalytic HER. Our simulations reveal that proton tunneling exhibits a substantial impact on the free energy profile of elementary PCET reactions in HER and, more importantly, provides new physical pictures for understanding pathways of the transferring proton overcoming kinetic barriers in the Volmer and Heyrovsky steps. We note here that we are not aiming to provide quantitatively exact reaction rate evaluations for the PCET elementary steps in this study. The major contribution of our work is the development of an integrated sampling framework for free energy calculations which can explicitly treat NQEs under an exact constant potential condition. We will first introduce the main idea and principles of our developed computational algorithm, and then present the major results elucidating the NQEs in electrocatalytic HER in the following sections.

Results

Methodology principles

Firstly, we introduce the principle of the GC-HMC algorithm proposed by this study. Considering a system with the coordinates of all particles and the total electron number represented by $\mathbf{R}$ and N_e, respectively, the GC ensemble partition function can be expressed as

$$\begin{aligned}\Xi(\beta, \mu_e) &= \sum_{N_e} \Lambda \int d\boldsymbol{R} \exp\left[-\beta(E(\mathbf{R}, N_e) - \mu_e N_e)\right] \\ &= \sum_{N_e} \exp(\beta\mu_e N_e) Q(\beta, N_e)\end{aligned} \tag{1}$$

where $\beta = \frac{1}{k_B T}$ is the inverse temperature, Λ is the prefactor generated by the integral of momenta degrees of freedom, $E(\mathbf{R}, N_e)$ and μ_e express the potential energy and the electrochemical potential of the external electronic reservoir in equilibrium with the system respectively, and $Q(\beta, N_e)$ refers to the canonical ensemble partition function (integral in the phase space) at a specific temperature β and with a total number of electrons N_e. For the exact GC ensemble condition, the work function of an instantaneous configuration will fluctuate around $-\mu_e$ during the simulation, rather than being fixed at $-\mu_e$ which corresponds to the situation using the GC-DFT method.

Sufficient configurational sampling of complex electrode/solvent interfacial environment is essential for studying PCET steps. Due to the issue of particle-number variations in GC conditions, MC[39,40] is a more practical method for open system simulations with particle insertion/deletion compared to MD[40,41]. We employ the HMC[42,43] method to improve the sampling efficiency with multi-particle displacements. Free energy profiles provide important physical insights into the thermodynamic and kinetic properties of PCET steps. The thermodynamic integration (TI) method[7,8,44] is appropriate for computing the free energy profiles with constraints on a defined RC. Considering the above requirements, a constrained HMC approach proposed in our previous study[45] is employed in this work. The details of the constrained HMC method are shown in the **Methods** section.

To achieve an exact constant potential condition, the constrained HMC method can be easily extended to a constrained GC-HMC method by incorporating an extra degree of freedom – the total electron number N_e of the surface models. We can sample N_e by the Metropolis algorithm with particle coordinates fixed, and the corresponding acceptance probability is

$$A(N_e'|N_e) = \min\left[1, \exp\left(-\beta\left(E(\mathbf{R}, N_e') - E(\mathbf{R}, N_e) - \mu_e(N_e' - N_e)\right)\right)\right] \tag{2}$$

For the exploration of particles' positions, we employ the constrained HMC method[45] at a fixed N_e value. The workflow of the GC-HMC algorithm is shown in Fig. 1a. An MC sampling trajectory begins with an initial structure characterized by the composite configuration $[\mathbf{R}, N_e]$ of the system. Three types of degrees of freedom are considered: the total number of electrons (N_e), the centroid of atomic coordinates ($\mathbf{R}$), and internal degrees of freedom within the quantized beads' configurations ($\mathbf{R}_\Delta^{(k)}$). We then randomly select which type of degrees of freedom to be perturbed by trial moves at each MC step, based on a random number ξ satisfying a uniform distribution within [0, 1]. We vary the total electron number N_e based on Eq. 2 to achieve a GC constant potential condition or perform HMC for the centroid of atomic positions ($\mathbf{R}$) to sufficiently sample the complex interfacial structure, or use the PIMC method to treat NQEs, by which we update $\mathbf{R}_\Delta^{(k)}$ based on the staging algorithm[46,47]. Estimators of targeted physical quantities are subsequently evaluated. We repeat the above process until reaching the required total MC step number, and finally obtain the ensemble average of interested physical quantities.

In fact, a potentiostat-based constant potential MD algorithm was proposed by Bonnet, Morishita, Sugino, and Otani in 2012[48], which is also a sampling approach with instantaneous work function fluctuations conforming with an exact grand canonical distribution, equivalent to the GC-HMC method proposed in our study. This scheme was later performed combined with Blue Moon ensemble-constrained MD simulations to obtain free energy profiles[49,50]. Liu group's recent review paper[51] also discussed the importance of work function fluctuation under the exact GC ensemble condition and developed a patch for VASP called CP-VASP[51], which realizes a constant potential condition with the potentiostat proposed by the original work[48]. If we aim to accomplish a constant pH condition in the future, our GC-HMC algorithm is easier to accommodate to variable proton-number sampling than the forementioned MD algorithm[48], which has to deal with the discontinuity issue of particle insertion/deletion. To fulfill a constant pH condition, the number of protons in the electrode/solvent system needs to be dynamically adjusted during sampling. This is similar to the strategy for maintaining a constant potential by varying N_e as discussed above, which could be implemented as an independent module in the computational framework (Fig. 1a) in our future study.

Since the NQEs play an important role even at room temperature, the Feynman PI algorithm[28,29] is employed to consider the quantum feature of protons in the PCET steps. The quantum GC ensemble partition function can be expressed as

$$\Xi_{qtm}(\beta, \mu_e) = \sum_{N_e} \exp(\beta\mu_e N_e) Q_{qtm}(\beta, N_e) \tag{3}$$

where $Q_{qtm}(\beta, N_e)$ refers to the quantum canonical ensemble partition function (its formulation is given by Eq. 12 in the **Methods** section). The expression of the quantum GC ensemble partition function $\Xi_{qtm}(\beta, \mu_e)$ is analogous to the classical one shown in Eq. 1, please refer to Supplementary Note 1 for detailed derivation of $\Xi_{qtm}(\beta, \mu_e)$. Combining the PIMC algorithm with the GC-HMC method, the quantum effect can be taken into account together with sufficient configurational sampling of the electrode/solvent interface. The details of the PIMC algorithm implemented in this study are shown in the **Methods** section. In the quantum case, the expression of the acceptance ratio of the total electron number N_e trial move is similar to Eq. 2, except that the potential energy $E(\mathbf{R}, N_e)$ in Eq. 2 is replaced by the average potential energy of all beads sharing the same electron number N_e in the PI formalism (refer to Supplementary Note 1 for detailed discussions).

Framework of our developed DP-N_e

A traditional MLP model, such as DP[30], typically substitutes atomic coordinates as inputs and infer the total energy and atomic forces of a modeling system. In this work, we introduce a new degree of freedom to input parameters: the total number of electrons N_e of our modeling interfacial system (Fig. 1b). To enable computing the work function

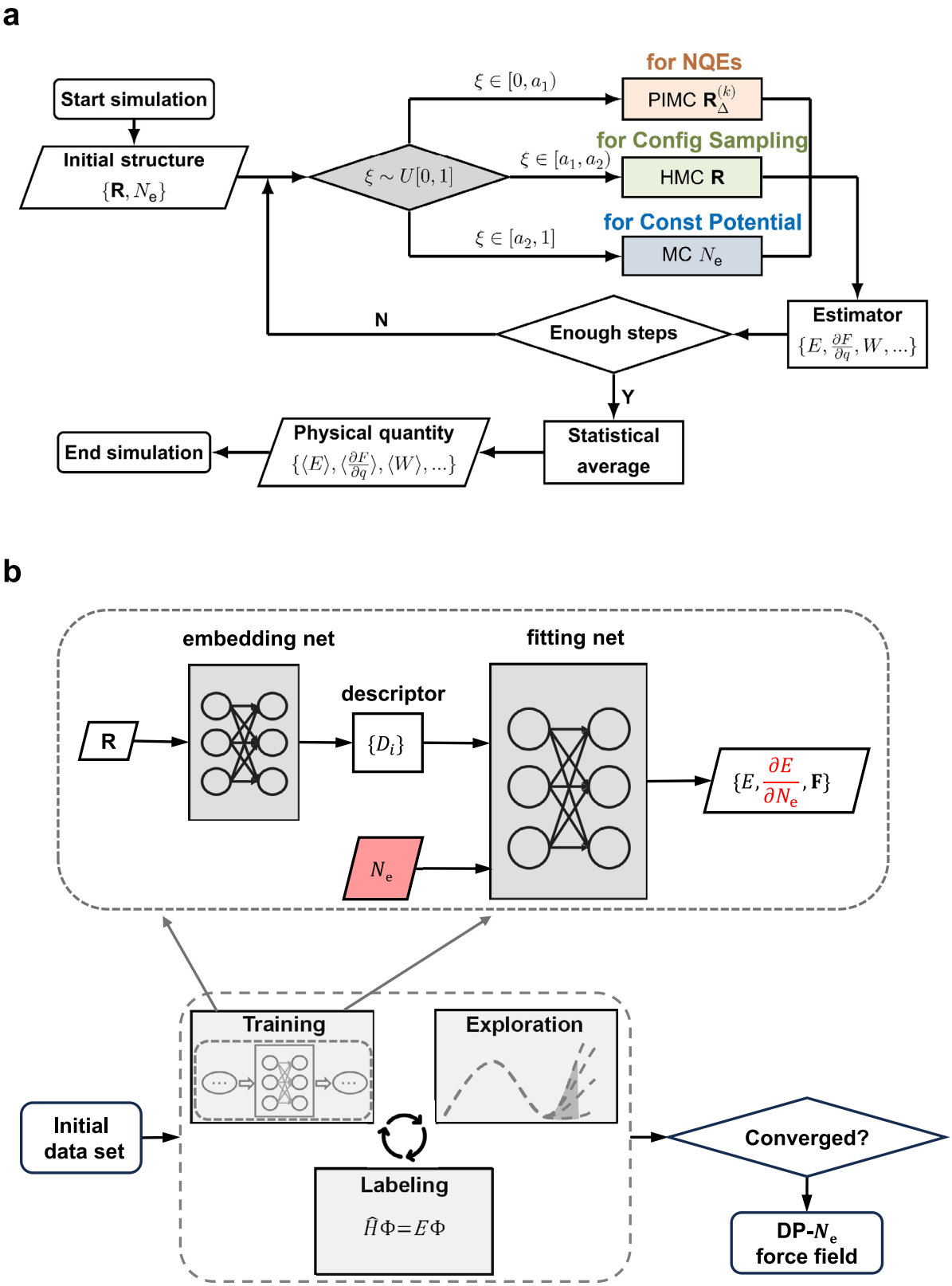

(W) of an instantaneous sampled configuration in the extended space $[\mathbf{R}, N_e]$, we include an additional output $\frac{\partial E(\mathbf{R},N_e)}{\partial N_e} = -W(\mathbf{R},N_e)$. For a valid GC ensemble sampling, it is essential to satisfy:

$$<\frac{\partial E(\mathbf{R},N_e)}{\partial N_e}>_{GC} = <-W(\mathbf{R},N_e)>_{GC} = \mu_e \quad (4)$$

where $<\cdot>_{GC}$ denotes the statistical GC ensemble average, details of which can be referred to the following results and Supplementary Note 4. Figure 1b shows the general framework of the DP-N_e model adopted in this study. Our developed DP-N_e MLP facilitates the sampling of GC ensembles with variable electron numbers. Chen et al. proposed a practical approach for machine-learning emulation derived from the GC-DFT method[14], which incorporates the electrode potential as a new

Fig. 1 | Workflow of the GC-(PI)HMC method and training workflow of the DP-N_e MLP. a Workflow of the GC-(PI)HMC method. The trial moves for different types of degrees of freedom are selected based on a preset ratio using a random variable ξ satisfying a uniform distribution within [0, 1], and the probabilities of making trial moves for the internal degrees of freedom within the quantized beads' configurations in PIMC ($\mathbf{R}_\Delta^{(k)}$), centroid atomic coordinates ($\mathbf{R}$), total number of electrons (N_e) are $a_1, a_2 - a_1, 1 - a_2$, respectively. **b** Construction framework and training workflow of the DP-N_e MLP adopted in this work. Initially, a data set is provided, followed by an iterative process which automatically goes through training, exploration, and labeling steps. The iteration is considered converged after the accurate sample percentage among the newly explored configurations is above 85%. The zoom-in schematic plot above the training workflow illustrates the construction framework of the DP-N_e force field. Atomic coordinates $\mathbf{R}$ of a modeling system are inputs for the embedding network generating descriptors $\{D_i\}$. The fitting network maps $\{D_i\}$ together with an extra degree of freedom N_e to the total energy E, atomic forces $\{\mathbf{F_i}\}$, and $\partial E/\partial N_e$ which relates to the work function of this extended configuration $[\mathbf{R}, N_e]$ as discussed in the following sections.

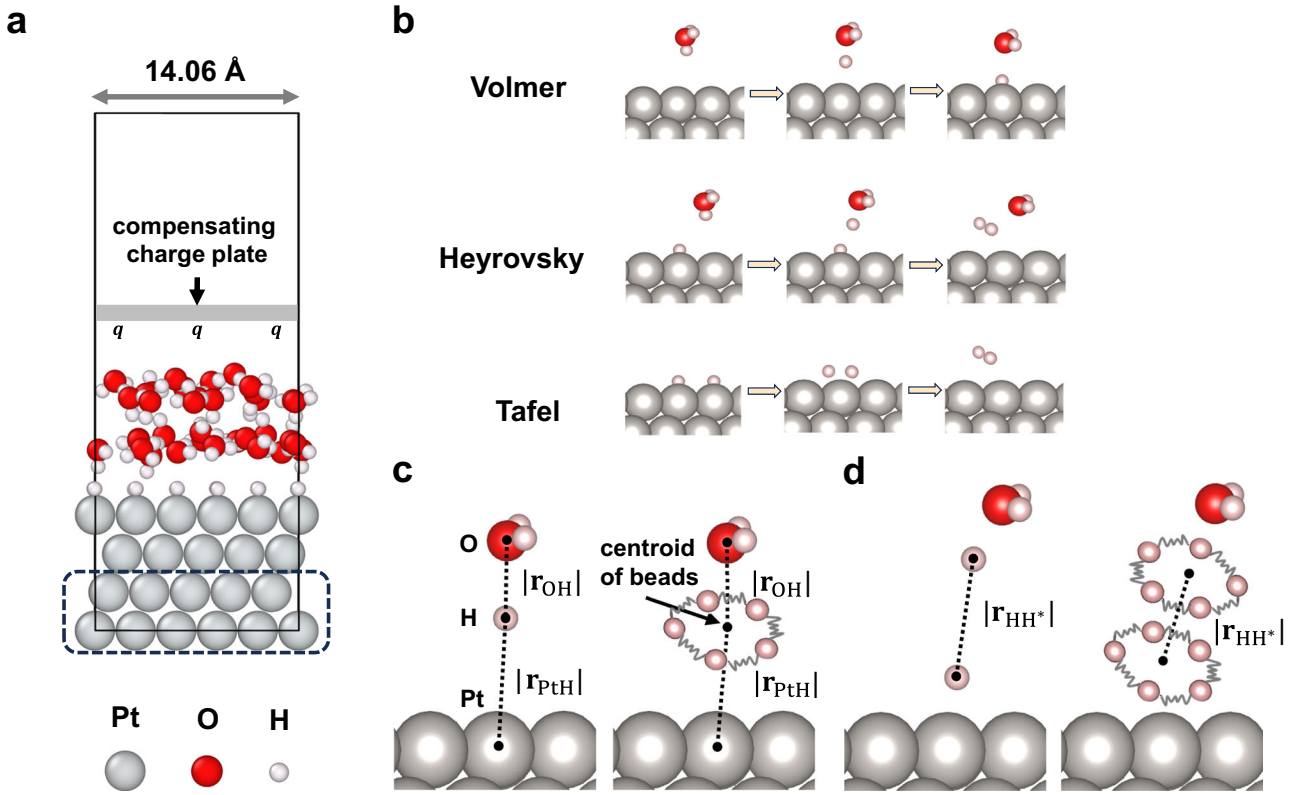

Fig. 2 | Atomic model construction, reaction pathways and RC definition. a Side view of the simulated (5 × 5) Pt (111) surface slab composed of four atomic layers. The interface model contains a water bilayer over 1 ML of adsorbed hydrogen. A compensating charge plate is placed in the vacuum region above the water solvation layer. The Pt atoms inside the black dashed rectangle are fixed along all simulation trajectories. **b** Schematic diagrams of the proton transfer pathways of three elementary reactions (Volmer, Heyrovsky, Tafel) involved in HER. Illustration of the key atoms relevant to the RC definitions of the (**c**) Volmer and (**d**) Heyrovsky steps for classical (left) and quantum (right) cases. Adsorbed hydrogen atoms and water molecules not directly participating in the investigated reactions are not displayed in these schematic plots for clarity.

degree of freedom into the input parameters. However, the construction of this machine-learning force field actually encounters the same issue as the GC-DFT approach, which does not perform an exact sampling of the microstates' distribution based on the GC partition function, but instead enforces a fixed work function constraint.

We validate the accuracy of our DP-N_e MLP by comparing the inferred energies and forces with the DFT results, and a good agreement on the testing dataset is achieved as shown in Supplementary Fig. 3. The total root mean square errors (RMSEs) of energies and forces on the testing dataset are 0.6 meV/atom and 57 meV/Å for configurations along the Volmer reaction path, and 1.1 meV/atom and 71 meV/Å for the Heyrovsky reaction case. Such small errors indicate the reliability of our DP-N_e force field model in describing the PES of HER steps with respect to the extended degrees of freedom $[\mathbf{R}, N_e]$.

Construction of the atomic interface model

We study the PCET steps involved in HER on a (5 × 5) Pt (111) surface slab composed of four atomic layers illustrated in Fig. 2a. The modeled electrode surface contains 100 Pt atoms with 1 monolayer (ML) hydrogen coverage at Pt atop sites[52,53]. No constraints or control is exerted on the adsorbed H* atoms during our sampling, and we do see the adsorbed H* atoms migration between the atop sites and the hollow or bridge sites along our sampled MC trajectories because of similar adsorption energies among different surface sites[12,54–60]. We also include two water layers (36 explicit water molecules) to take account of the solvation effect and provide proton donors. Tests for the influence of water-layer numbers on the free energy results are shown in Supplementary Note 11. A vacuum region of 15 Å thickness is further added above the water layers in order to decouple periodic images of the slab model. Since we adjust the total electron number of the interface system in our GC-HMC algorithm, compensating charge has to be included to maintain the overall charge neutrality of the supercell under a periodic boundary condition (PBC). We employ the scheme of placing a compensating charge plate in the vacuum region right above the water solvation layer to mimic an effective electric double layer at the electrode/solution interface, analogous strategies

can be found in earlier theoretical work[33,61,62]. We realized the above function in the first-principles package Atomic-orbital Based Ab-initio Computation at UStc (ABACUS)[63,64] used in this study, consistent with the corresponding algorithm implementation in the popular DFT code Quantum ESPRESSO (QE)[65,66]. We further benchmark our calculated electrostatic energy profiles with the QE results on a testing interface model and discuss the potential influence caused by varying the compensating charge plate's positions. Details can be found in Supplementary Note 2.

The HER process starts with a Volmer reaction, which is a PCET step of a proton's adsorption forming an H*. Following this, the evolution of an H_2 molecule can proceed along two distinct pathways: the Volmer-Tafel or the Volmer-Heyrovsky mechanisms. The proton transfer pathways of the Volmer, Heyrovsky, and Tafel steps are illustrated in Fig. 2b. We note that the Tafel step, characterized as a chemical (instead of an electrochemical) reaction with negligible charge transfer across the interface, is beyond the scope of PCET steps, thus is not extensively discussed in the main text. We present our investigation of the NQEs on the Tafel reaction in Supplementary Note 10.

We need to define reasonable RCs for different types of reaction paths so that we could drive reactions and perform the mean force integration by our GC-(PI)HMC. In the present work, we employ the difference of bond distances $|\mathbf{r}_{PtH}|$ and $|\mathbf{r}_{OH}|$ as the RC q_{Volmer} for the Volmer reaction (Eq. 5), in which $|\mathbf{r}_{PtH}|$ is the distance between the Pt atom for H adsorption and the transferring proton, and $|\mathbf{r}_{OH}|$ is the distance between the proton donating oxygen (belonging to an H_2O molecule above the Pt site) and the transferring proton (illustrated in the left panel of Fig. 2c). For the Heyrovsky reaction, we define the RC $q_{Heyrovsky}$ as the distance $|\mathbf{r}_{HH^*}|$ between the two hydrogen atoms forming the H_2 molecule (Eq. 6), the definition is schematically depicted in the left panel of Fig. 2d.

$$\text{Volmer RC}: \ q_{Volmer} = |\mathbf{r}_{PtH}| - |\mathbf{r}_{OH}| \tag{5}$$

$$\text{Heyrovsky RC}: \ q_{Heyrovsky} = |\mathbf{r}_{HH^*}| \tag{6}$$

Similar types of RCs have been widely used in many previous studies on catalytic mechanisms for electrochemical systems[11,12,16]. In the quantum situations for studying NQEs, the transferring H in the Volmer step and the two combining H atoms in the Heyrovsky step are quantized as beads configurations isomorphic to a ring-polymer model[20,21,23,67], we then treat the centroid of the corresponding ring-polymer beads (illustrated in the right panels of Fig. 2c, d) as the positions of the quantized H atoms[21,23]. The impact of considering NQEs for more protons in the explicit water solution is discussed in Supplementary Note 12.

Setup of DFT calculations

DFT calculations in this work are utilized to train ML force fields, rather than for direct MC sampling. All DFT calculations in this work are performed using a first-principles calculation software ABACUS (version 3.4.0)[63,64] with a main feature of employing numerical atomic orbitals (NAO) as the basis set, which is capable of performing efficient DFT calculations for more than hundreds of atoms in a supercell. In addition, the function of an adjustable total number of electrons with a compensating charge plate, whose position is also configurable, is implemented in the ABACUS code (Supplementary Note 2). We thus employ ABACUS to perform all of the ab initio calculations for labeling the DP-N_e training dataset throughout the work.

The norm-conserving pseudopotentials are adopted with the valence electron configurations: [H]$1s^1$, [O]$2s^22p^4$, and [Pt]$5s^25p^65d^86s^2$. We use the generalized gradient approximation (GGA) in the form of the Perdew–Burke–Ernzerhof (PBE) version[68] for describing the exchange-correlation functional. Specifically, we choose 2s1p, 2s2p1d, and 4s2p2d1f NAO basis sets with radius cutoffs as 6, 7, and 7 Bohr, respectively for H, O, and Pt elements. The kinetic energy cutoff is set to 100 Ry (1360 eV). We employ the PBC for modeling the Pt/H_2O interface supercell, and the k-point mesh for sampling the Brillouin zone of the slab model with dimensions of 14.06 Å × 14.06 Å × 30.89 Å is set as 2 × 2 × 1. A dipole correction[69] is included in our DFT calculations as well due to the net dipole of the interface model especially at charged states representing an electrochemical reducing condition. We use the Gaussian smearing method with a width of 0.02 Ry. We also apply Grimme's D3 dispersion correction[70] to take account of the long-range van de Waals interaction effect.

Statistical results of potential and charge variations from our GC sampling

Since the PCET steps involve electron transfer across interfaces, the activation energies of Volmer and Heyrovsky steps have a dependence on applied potentials. It is through the work function that we can establish a connection between the reduction voltage U relative to the standard hydrogen electrode (φ_{SHE}, ~ 4.4 V vs the vacuum level[71,72]) as follows:

$$U = \frac{W}{|e|} - \varphi_{SHE} \tag{7}$$

where $|e|$ means the unit charge, and the work function $W(\mathbf{R}, N_e)$ of an instantaneous microstate, sampled in our GC-(PI)HMC trajectory within the extended $[\mathbf{R}, N_e]$ configurational space, can be obtained from $\frac{\partial E(\mathbf{R}, N_e)}{\partial N_e}$ as introduced in the above section (refer to Supplementary Note 4 for detailed DFT validations). We are able to achieve different electrochemical reducing conditions in the GC sampling for this open system by adjusting the electrochemical potential parameter μ_e of the external electronic reservoir (shown in Eq. 1), equivalent to the potentiostat scheme proposed by an earlier theoretical work[48]. We thus can compute the free energy profiles of the investigated PCET steps at different applied potentials. Figure 3a shows that the GC ensemble average $<W(\mathbf{R}, N_e)>_{GC}$ equals to the controlling parameter $-\mu_e$, which is consistent with Eq. 4 and justifies the validity of our GC sampling. The magnitude of the work function fluctuation range is also consistent with the earlier results obtained by the above-mentioned potentiostat scheme (~ ± 0.5 eV)[48]. The modeled system corresponds to the Volmer step with q_{Volmer} = 0.21 Å at μ_e = − 3.5 eV vs vacuum (U = − 0.9 V vs SHE).

The modeled system's total electron number N_e also fluctuates around an average value, as shown in Fig. 3b, and exhibits a normal distribution (Supplementary Note 5), satisfying the GC ensemble distribution. We use the extra electron number (N_e^{extra}) added/subtracted to/from the Pt/H_2O interface model to represent the total electron number for clarity. The average value $<N_e>_{GC}$ corresponds to the system's charge state at a specific applied potential condition. We need to emphasize that an exact thermodynamic simulation of an electrochemical open system should obey the fundamental principle of the GC ensemble distribution (Eq. 1), where N_e and $W(\mathbf{R}, N_e)$ are a pair of conjugate thermodynamic variables of a microstate. A correction formulation of GC sampling should exhibit the feature that neither N_e nor W of sampled microstates is fixed along a simulation trajectory, while the ensemble average $<W(\mathbf{R}, N_e)>_{GC}$ equals to the controlling parameter $-\mu_e$ of an external electronic reservoir. An analogous concept applies to the case of an isothermal-isobaric NPT ensemble sampling, where neither volume V nor the pressure $P(\mathbf{R}, V)$ of the sampled microstates is fixed, while the average pressure $<P(\mathbf{R}, V)>_{NPT}$ equals to the setup external pressure. The above fundamental principle is rarely treated exactly in the electrocatalytic simulation community, where the fixed charge or fixed potential schemes were commonly adopted in the potential energy or free energy calculations for electrochemical PCET steps.

https://doi.org/10.1038/s41467-025-58871-7

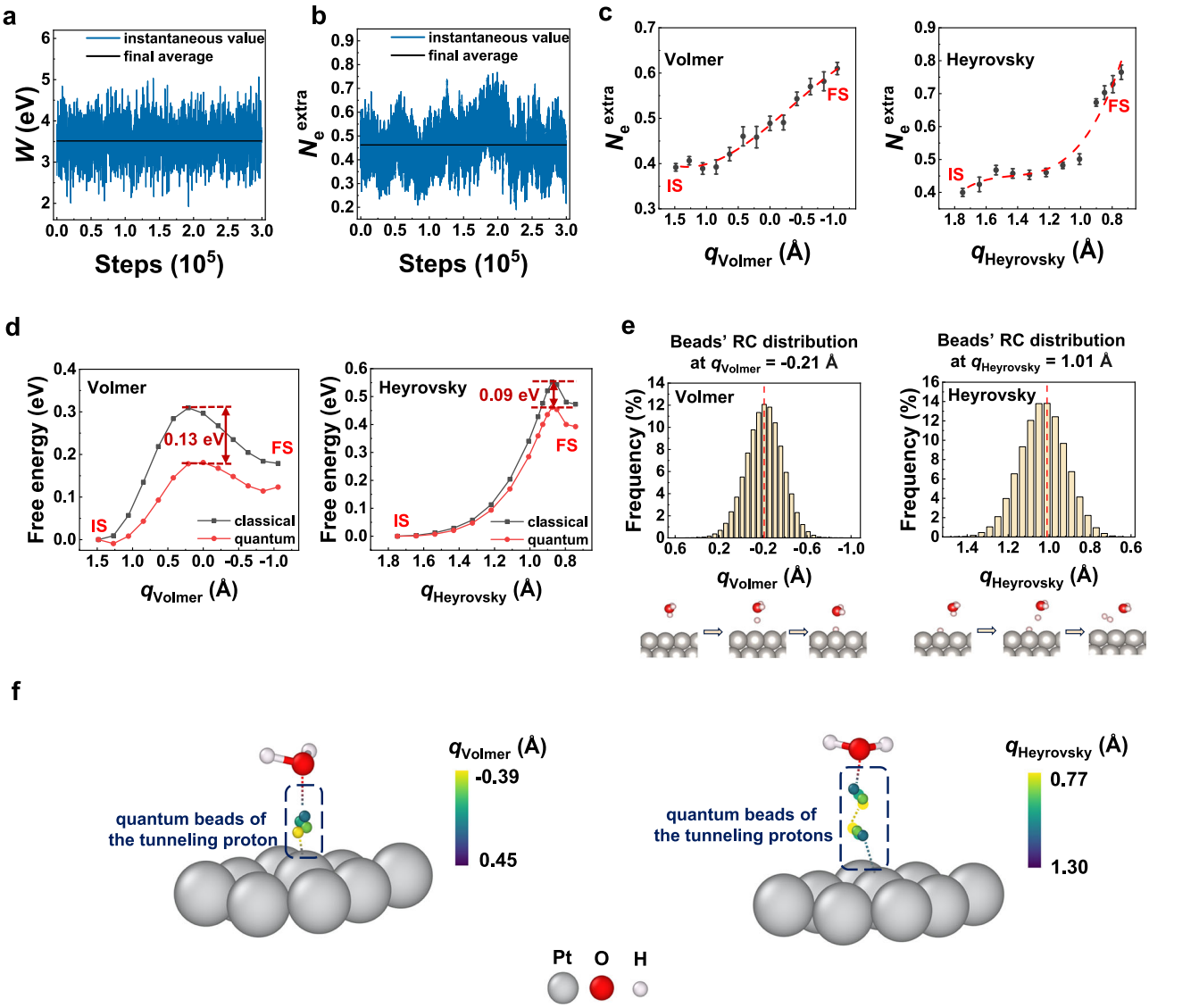

Fig. 3 | Sampling results and NQEs on free energy and beads distribution. **a** Work function and (**b**) total electron number fluctuation with respect to MC steps of the Volmer reaction with an RC fixed at q_{Volmer} = 0.21 Å. The extra electron number added/subtracted to/from the model (N_e^{extra}) is used to represent the total electron number for clarity. Blue curves show the instantaneous values, and black lines are the final averages along complete sampling trajectories. **c** Total electron number (represented by N_e^{extra}) change along the reaction path from IS to FS of classical Volmer and Heyrovsky simulations. Error bars represent standard errors (refer to Supplementary Note 6 for the definition) from 15 (Volmer) or 10 (Heyrovsky) independent simulations. Red dashed curves are simply guidelines showing the trend of electron number variation with respect to RC. **d** Classical and quantum free energy profiles with respect to the defined RC of the Volmer and Heyrovsky PCET steps. **e** RC distribution associated with the ring-polymer beads in the PI simulations of Volmer and Heyrovsky reactions. Red dashed vertical lines are the constrained RC values defined for the proton beads' centroid in our PIMC, which also correspond to the constrained RC values in classical simulations without RC spreading. **f** Structural plots explicitly showing the spreading beads of the transferring protons or hydrogen atoms at q_{Volmer} = 0.0 Å for the Volmer reaction and $q_{Heyrovsky}$ = 0.95 Å for the Heyrovsky reaction. Adsorbed hydrogen atoms and Pt layers not directly participating in the studied reactions are not displayed here, and only one water molecule (the proton donor) remains in the plot for clarity. Only part of the 16 ring-polymer beads are shown. All results in this figure are obtained under a specific reduction potential of $U = -0.9$ V vs SHE (or $\mu_e = -3.5$ eV vs vacuum) at T = 300 K. Source data are provided as a Source Data file.

A gradual increase of total electron number is observed from the IS to the FS along the reaction pathways of both the Volmer and Heyrovsky mechanisms (shown in Fig. 3c), which is as expected because the electrode slab needs to keep acquiring electrons to facilitate the progress of reduction reactions when in equilibrium with an electronic reservoir at a constant electrochemical potential. The error bars in Fig. 3c denote standard errors (SE) of average N_e^{extra} derived from 15 (Volmer) or 10 (Heyrovsky) independent simulations for each case at $U = -0.9$ V vs SHE (refer to Supplementary Note 6 for the definition of SE). We further conduct detailed calculations to examine the relationship of charge states of the Volmer step's IS and FS with applied potentials (Supplementary Note 6). The results exhibit a consistent trend that a more negative potential leads to larger electron numbers in the modeled system, indicating a reasonable electronic response in PCET reactions that a stronger reducing driving force requires a higher concentration of electrons in the system.

Impact of NQEs on activation energies of PCET steps in HER

We obtain the free energy profiles of the Volmer and Heyrovsky PCET steps at $\mu_e = -3.5$ eV vs vacuum ($U = -0.9$ V vs SHE), presented in Fig. 3d, by numerically integrating the mean forces at different RCs along the reaction paths[23,45,73]. To further investigate the impact of NQEs on these PCET-free energies, we implement the PIMC algorithm into the GC-HMC method (illustrated by the workflow plot in Fig. 1a).

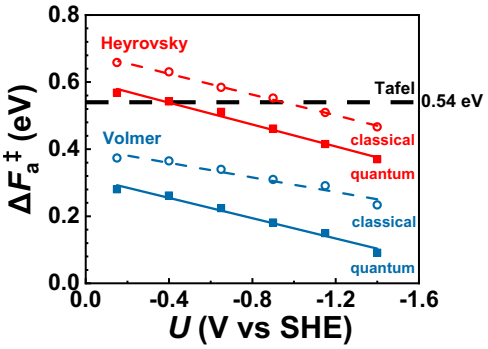

Fig. 4 | Activation free energy results with respect to electrochemical potentials. Activation free energy results of Volmer and Heyrovsky mechanisms with respect to electrochemical potentials under classical and quantum situations at $T = 300$ K. Blue (Red) hollow circles and solid squares represent the Volmer (Heyrovsky) reaction for the classical and quantum cases, respectively. Solid and dashed lines derived from a linear fitting simply perform as guidelines illustrating the trend. The black dashed line represents the activation energy result (0.54 eV) of the Tafel reaction, which does not change with respect to voltage variation, and has almost identical values under classical and quantum conditions. Source data are provided as a Source Data file.

We then compare the free energy results between the classical and quantum situations. The computational details of our sampling calculations are presented in **Methods** section. The quantitative influence on the activation free energies ($\Delta F_a^{\ddagger}$) of the Volmer and Heyrovsky steps are 0.13 eV and 0.09 eV, respectively (at $U = -0.9$ V vs SHE) upon incorporating NQEs of the transferring protons in these PCET catalytic steps (Fig. 3d). When considering NQEs in the free energy calculations, the predicted activation energies exhibit a notable decrease, leading to a non-negligible enhancement of the investigated PCET reaction rates compared to the results of classical cases. The above results indicate that reaction rates could be underestimated by approximately 50–100 folds at $T = 300$ K if we employ the traditional view of treating protons as classical particles, based on the transition state theory (TST) expression:

$$k_{TST} = \frac{k_B T}{h} e^{-\frac{\Delta F_a^{\ddagger}}{k_B T}}. \quad (8)$$

For example, at $U = -0.9$ V vs. RHE, we have k_{TST}(classical, Volmer) = 4.00×10^7 /s, k_{TST}(quantum, Volmer) = 5.67×10^9 /s for the Volmer PCET step, and k_{TST}(classical, Heyrovsky) = 3.30×10^3 /s, k_{TST}(quantum, Heyrovsky) = 1.12×10^5 /s for the Heyrovsky PCET step. However, it is also well known that the TST expression is just an approximation for the rate constants due to a lack of dynamic consideration at the dividing surface of a reaction path. More rigorously, we should discuss the validity of the k_BT/h pre-factor in the TST formula or the impact of the dynamic correction κ on this pre-factor (mainly caused by the re-crossing effect at the dividing surface in real dynamics). We admit that the precise calculations of the dynamic correction in the quantum case (considering NQEs) $\kappa_{quantum}$ and that in the classical case (without NQEs) $\kappa_{classical}$ are beyond the scope of our research. Many previous theoretical studies show that both $\kappa_{quantum}$ and $\kappa_{classical}$ are not far from unity (in the range of 0.5 ~ 1), implying that it is likely to be a minor correction to the TST rate constant[74–76]. More importantly, if we look at the ratio $\kappa_{quantum}/\kappa_{classical}$, which is actually the key quantity we are interested in (as we only focus on the qualitative NQEs influence on the rate constants), this ratio is even closer to 1 (in the range of 0.7 ~ 1)[74–76]. We thus can see that the exponential term $e^{-\frac{\Delta F_a^{\ddagger}}{k_B T}}$ largely determines the reaction rate difference between the situations with vs without NQEs in our work, justifying the catalytic insights provided by our free energy calculations. We need to emphasize that although we provide estimated PCET reaction rates, the main goal of our work is not to pursue quantitatively exact rate constants for elementary steps in HER. We focus on statistical sampling methods development and aim to demonstrate the importance of NQEs in room-temperature electrocatalysis by employing our sampling framework.

We realize some readers may raise a question here that, since DFT calculations with different setup typically exhibit an uncertainty or deviation range of about 0.1–0.2 eV in describing energetics of electrocatalytic steps, is the reported quantitative NQEs' impact of 0.1–0.15 eV (shown in Fig. 3d and Fig. 4) on PCET activation energies reliable or of physical meaning in this work? The basic logic of our response is that, as we keep all of the first-principles calculations consistent within this study and our adopted DFT setup also follows a routine of simulations in electrocatalysis, the uncertainty caused by inconsistent first-principles calculation setup can be excluded, meaning that the important qualitative impact of NQEs on HER PCET steps is expected to persist if other ab-initio setup schemes are employed. We actually find that earlier theoretical predictions (all performed in a classical situation) of the PCET activation energies in electrocatalytic HER at Pt surfaces were consistently higher than those from experimental measurements[35–38]. The NQEs, thus, could be a key factor for reconciling the above discrepancy, as revealed by our computational study which explicitly deals with the NQEs under an exact GC ensemble sampling.

Proton tunneling originates from the intrinsic quantum nature, which is already demonstrated to be remarkable even at room temperature for the HER PCET steps. To achieve a clearer and qualitative understanding of the transferring proton's quantum feature, we analyze the quantum beads expansion for the states at near-TS RC in the Volmer path (q_{Volmer} = -0.21 Å) and the Heyrovsky path ($q_{Heyrovsky}$ = 1.01 Å) at $U = -0.9$ V vs SHE in Fig. 3e. Let's first consider in a classical picture, the positions of the transferring protons or hydrogen atoms are essentially mass points obeying the constraint of a specific RC. If we plot the RC value of each sampled configuration in a GC-HMC trajectory, all of which must fall onto a single value, corresponding to the red dashed vertical lines in Fig. 3e. However, the situation is quite different in the quantum case, since a proton or hydrogen atom can "split" into multiple beads in the PI algorithm, the "uncertainty" of a micro particle's position just reflects its quantum feature. Therefore, if we do the statistics of each bead configuration's RC value along our GC-PIHMC sampling trajectory and plot the histogram (Fig. 3e), the RC distribution would spread around an average number (actually equals to the constrained RC value defined for the proton beads' centroid). We can clearly see that the quantum-treated transferring proton exhibits an IS-TS-FS mixed feature at the TS of the Volmer or the Heyrovsky path, as illustrated by the schematic atomic structures underneath the histogram plots (Fig. 3e). This observation indicates a sharp contrast with the classical deterministic understanding of transferring protons along PCET paths, and further explains the lowered activation energy due to the tunneling effect. This is because the TS in the PIMC simulations also mixes with ring-polymer beads with RCs corresponding to IS and FS, which have lower potential energies than the classical TS configurations.

A more direct configurational visualization of the spreading beads of the transferring protons or hydrogen atoms in the Volmer and Heyrovsky path are presented in Fig. 3f. We conduct a quantum PI sampling at a specific near-TS configuration where the coordinates of all classical particles and the centroids of the quantized H are fixed, with the relative positions of the quantized H ring-polymer beads (or considered as the internal degrees of freedom within a quantized particle) being sufficiently sampled by the PI algorithm. We randomly choose a specific configuration of the spreading beads and show the structure plots in Fig. 3f, which exhibits a considerable uncertainty in

the quantized proton's or H atom's position and an unusual feature that IS and FS configurations are mixed in the TS sampling by the PI simulations. For example, the IS-like configuration (H^+_{sol} + H*), denoted by the blue color, and the FS-like configuration (H_2), highlighted by the yellow color, coexist in the Heyrovsky TS PIMC sampling (the right panel of Fig. 3f), resulting in an emergence of the tunneling behavior (note that we only show part of the 16 ring-polymer beads for clarity). We thus can obtain a qualitative physical picture that the transferring proton or H atom exhibits wave-like quantum characteristics, facilitating the particles to tunnel through classical barriers along the PCET pathways in HER, leading to a remarkable activation energy reduction compared to the classical simulations. The NQEs revealed by our theoretical work thus contribute new physical insights into the fundamental understanding of PCET dynamics in electrocatalytic HER.

Insights into the HER mechanism inspired by the consideration of NQEs

The above results reveal the exotic quantum behavior of the transferring protons during PCET processes. We are now interested in the impact of NQEs on our understanding of the electrocatalytic HER mechanism. Two well-known reaction pathways compete with each other, that is, the Volmer-Heyrovsky pathway against the Volmer-Tafel pathway. Figure 4 shows the activation energies of the Volmer, Heyrovsky, and Tafel elementary steps with respect to applied electrochemical potentials for both of the classical and quantum situations. We note that the activation energy of the non-electrochemical Tafel step is expected to exhibit negligible dependence on applied potentials, we thus plot its activation energy as a constant value (derived from our calculations with details shown in Supplementary Note 10) in Fig. 4. Our classical activation energy results are in good agreement with a recent computational work[12] numerically, where similar activation energies of both the Tafel step (0.53 eV) and the Volmer step (0.25–0.50 eV) were reported in their study within the relevant voltage range investigated in this work, justifying our GC-HMC calculations under the classical situation. If the transferring proton is treated as a classical particle, the Volmer-Tafel path is more likely to dominate the H_2 production under the electrochemical condition of voltage $U \geq -0.9$ V vs SHE. However, due to the proton tunneling behavior resulting from its intrinsic quantum nature, more exact activation energies of the Heyrovsky step, considering NQEs, are ~0.1 eV lower than those derived from the classical cases. Since the Tafel steps are almost not affected by NQEs (discussed in Supplementary Note 10), we can see from Fig. 4 that the transition point from the Volmer-Tafel path to the Volmer-Heyrovsky path is significantly shifted to a less reducing potential region by a difference of 0.5 V, indicating a tendency of the electrochemical Heyrovsky step suppressing the chemical Tafel step toward a smaller overpotential condition. An experimental-theoretical-joint analysis[77] claimed that the Volmer-Heyrovsky path is likely to dominate over the Volmer-Tafel path. While in another recent theoretical work raised by Kronberg et al. [12], the authors conducted CMD simulations only for the Volmer and Tafel steps and did not perform the free energy calculations for the Heyrovsky step thus discussion on the competitive relationship between the Volmer-Tafel vs. Volmer-Heyrovsky mechanisms was incomplete. Our work investigates the free energy profiles for all three elementary steps in HER (Volmer, Heyrovsky, and Tafel), and we find that the Heyrovsky step indeed gets more favorable compared to the Tafel step upon considering NQEs by our GC-PIHMC calculations as shown in Fig. 4, consistent with the statement from the previous work[77]. At the end, we also need to point out possible limitations inherent in the mean-force integration method for free energy profile calculations under constrained sampling algorithms. Since the solvent structures are sampled independently at each RC along the reaction pathway, our constrained HMC approach may overestimate the solvent reorganizations leading to a softened potential dependence of PCET activation energies in Fig. 4[12]. In our work, the free energy profile calculations are for the PCET elementary steps, and the IS and FS at electrode surfaces along PCET paths in our thermodynamic integration approach are not exactly consistent with the reactant state and the product state of the overall reaction ($H^+_{sol} + e^- \rightarrow 1/2\ H_2$(gas)). In addition, a constant pH condition is not implemented in our current approach, meaning that a non-negligible pH change would occur along our modeled elementary PCET step (refer to the next Section for more discussions). Regarding the above limitations, our computed free energy change of the overall reaction cannot be directly compared to that of the experiments.

Discussion

In this work, we employ our proposed GC-(PI)HMC sampling framework, assisted by a MLP adapted for electrochemistry, to reveal a non-negligible role of NQEs in computational work to achieve an exact quantitative description of electrochemical mechanisms, which is also consistent with earlier studies reviewed at the beginning of this article that NQEs exhibit remarkable influence in many chemical/materials systems[19–23] even at room temperature.

On the basis of this MC framework, we emphasize that the good expandability of our sampling workflow provides convenience for incorporating more physical factors in future code development. For example, the MC sampling for proton number variation, to achieve a constant pH condition, can be implemented as a new sampling branch in the workflow shown in Fig. 1a, which is an independent module and does not affect the programs of the other sampling functions for different types of degrees of freedom.

More importantly, the physical insight of proton tunneling provided by our simulations based on an exact constant potential GC sampling can be extended to broader scenarios in electrocatalysis, including ORR, CO_2RR, or nitrogen reduction reaction (NRR) systems. We may find similar qualitative NQEs impact on the kinetics of elementary PCET steps, which may reshape our fundamental understanding on electrocatalytic reactions. Our computational work thus highlights the importance of incorporating protons' NQEs in modeling PCET steps existing ubiquitously in energy conversion systems.

At the end, we need to point out a few limitations of our current computational framework. First, the thermodynamic integration method used in our approach produces free energy profiles, which are just thermodynamic results and lack realistic dynamic information. Second, the adiabatic approximation employed in this work ignores the non-adiabatic effect for now, which could be an important factor worthy of investigation in certain PCET reactions. The non-adiabatic effect would likely increase the effective activation energy slightly in both the classical and quantum cases especially when the non-adiabatic electronic coupling is small around the dividing surface region. However, it is still an open question about the relative magnitudes of the non-adiabatic effect on the effective activation energy shifts comparing the situations with vs. without NQEs. Third, as we employ the TI method to compute the free energy profiles along a defined RC, it is important to choose an appropriate RC representing the reaction progress. We acknowledge that the current version of our program is unavailable to support certain types of PCET simulations involving concerted multiple-proton transfers, and we are working on the implementation of more types of RC in our framework now. Moreover, the MC sampling performed by our proposed workflow requires training and the construction of an ML force field. Certain complex electrochemical systems may need exploring a larger configurational space, which could increase the cost of preparing a robust ML force field.

Methods

Methodology of the constrained HMC algorithm and derivations

For a system with all particle positions $\mathbf{R}$ and potential energy $U(\mathbf{R})$, we define a RC $q = f(\mathbf{R})$ to monitor the reaction process, and the reaction mechanism can be explored via MC simulations at different fixed q values using the constrained HMC algorithm[45]. The key idea of the

algorithm is to integrate the RC after a coordinate transformation and sample the rest two types of degrees of freedom with the corresponding two types of MC schemes. The procedures of the algorithm can be divided into the following three steps:

a. Apply an appropriate coordinate transformation on $\mathbf{R}$ to obtain general coordinates $\mathbf{q}=(q, \mathbf{q}_{\text{trans}}, \mathbf{q}_{\text{primit}})$, where $\mathbf{q}_{\text{trans}}$ and $\mathbf{q}_{\text{primit}}$ represent the transformed coordinates related to the RC and the primitive coordinates maintained the same in the transformation, respectively. Then we integrate the RC in the probability density of $q=s$ as follows

$$\begin{aligned}P(s) &= \frac{\Lambda}{Q(\beta, N_e)}\int d\mathbf{R}\exp\left[-\beta E(\mathbf{R}, N_e)\right]\delta(q-s)\\ &= \frac{\Lambda}{Q(\beta, N_e)}\int d\mathbf{q}\exp\left[-\beta\widetilde{E}(\mathbf{q}, N_e)\right]\delta(q-s)\mathcal{J}(\mathbf{q})\\ &= \frac{\Lambda}{Q(\beta, N_e)}\int dq d\mathbf{q}_{\text{trans}} d\mathbf{q}_{\text{primit}}\exp\left[-\beta\widetilde{E}(\mathbf{q}, N_e)\right]\delta(q-s)\mathcal{J}(q, \mathbf{q}_{\text{trans}})\\ &= \frac{\Lambda}{Q(\beta, N_e)}\int d\mathbf{q}_{\text{trans}}\mathcal{J}(s, \mathbf{q}_{\text{trans}})\int d\mathbf{q}_{\text{primit}}\exp\left[-\beta\widetilde{E}\left(s, \mathbf{q}_{\text{trans}}, \mathbf{q}_{\text{primit}}, N_e\right)\right]\end{aligned} \tag{9}$$

where $\mathcal{J}(\mathbf{q})$ is the Jacobian related to the coordinate transformation and $\mathcal{J}(\mathbf{q})=\mathcal{J}(q, \mathbf{q}_{\text{trans}})$.

b. The primitive coordinates $\mathbf{q}_{\text{primit}}$ together with the particle momenta $\mathbf{p}_{\text{primit}}$ are combined to obtain the partial Hamiltonian $\mathcal{H}(\mathbf{p}_{\text{primit}}, \mathbf{q}_{\text{primit}})$ used in the HMC scheme[42,43].

c. Select the sampling type of degrees of freedom at random based on the preset ratio and sample these degrees of freedom with the rest ones fixed. Specifically, $\mathbf{q}_{\text{trans}}$ evolves via the usual Metropolis scheme, and the acceptance probability is

$$\begin{aligned}&A(\mathbf{q}'_{\text{trans}}|\mathbf{q}_{\text{trans}})\\ &= \min\left\{1, \frac{\mathcal{J}(s, \mathbf{q}'_{\text{trans}})}{\mathcal{J}(s, \mathbf{q}_{\text{trans}})}\exp\left[-\beta\left(\widetilde{E}\left(s, \mathbf{q}'_{\text{trans}}, \mathbf{q}_{\text{primit}}, N_e\right)-\widetilde{E}\left(s, \mathbf{q}_{\text{trans}}, \mathbf{q}_{\text{primit}}, N_e\right)\right)\right]\right\}\end{aligned} \tag{10}$$

and $\mathbf{q}_{\text{primit}}$ evolves via the HMC scheme and the acceptance probability is

$$A\left(\mathbf{q}'_{\text{primit}}|\mathbf{q}_{\text{primit}}\right) = \min\left\{1, \exp\left[-\beta\left(\mathcal{H}\left(\mathbf{p}'_{\text{primit}}, \mathbf{q}'_{\text{primit}}\right)-\mathcal{H}\left(\mathbf{p}_{\text{primit}}, \mathbf{q}_{\text{primit}}\right)\right)\right]\right\} \tag{11}$$

The workflow of the constrained HMC method is shown in Fig. 1a and more details can be referred to our earlier theoretical work[45].

Methodology of the PI algorithm and derivations

Consider the same system in the above section, we represent the masses of all particles with a diagonal matrix $\underline{\boldsymbol{m}}$. In quantum mechanics, the partition function of a system is expressed as the trace of a density operator, which can be derived as follows using a factorization formalism proposed by Feynman[28,29]

$$\begin{aligned}Q_{\text{qtm}}(\beta, N_e) &= \text{Tr}\left[\exp(-\beta\hat{\mathcal{H}})\right]\\ &= \lim_{P\to\infty}\text{Tr}\left[\exp(-\beta\hat{\mathcal{H}}/P)^P\right]\\ &= \lim_{P\to\infty}\int d\mathbf{R}^{(1)}\cdots d\mathbf{R}^{(P)}\left\langle\mathbf{R}^{(1)}\right|\exp(-\beta\hat{\mathcal{H}}/P)\left|\mathbf{R}^{(2)}\right\rangle\\ &\quad\times\cdots\times\left\langle\mathbf{R}^{(P-1)}\right|\exp(-\beta\hat{\mathcal{H}}/P)\left|\mathbf{R}^{(P)}\right\rangle\left\langle\mathbf{R}^{(P)}\right|\exp(-\beta\hat{\mathcal{H}}/P)\left|\mathbf{R}^{(1)}\right\rangle\\ &= \lim_{P\to\infty}\Lambda_P\int d\mathbf{R}^{(1)}\ldots d\mathbf{R}^{(P)}\exp\left\{-\beta\sum_{k=1}^{P}\left[\frac{1}{2}\omega_P^2\left(\mathbf{R}^{(k+1)}-\mathbf{R}^{(k)}\right)^T\underline{\boldsymbol{m}}\left(\mathrm{R}^{(k+1)}-\mathbf{R}^{(k)}\right)\right.\right.\\ &\quad\left.\left.+\frac{1}{P}E\left(\mathbf{R}^{(k)}, N_e\right)\right]\right\}\Big|_{\mathbf{R}^{(1)}=\mathbf{R}^{(P+1)}}\end{aligned} \tag{12}$$

where the subscript "qtm" means quantum, P is the number of beads, $\mathbf{R}^{(k)}$ denotes the particles' positions of the ring-polymer bead with an index number k, Λ_P is the prefactor generated by the Gaussian integral when dealing with the momentum operators in the PI formulation, and $\omega_P=\sqrt{P}/\beta\hbar$ is the chain frequency of the adjacent harmonic coupling in the ring-polymer model. The above formalism describes a quantum system through an isomorphic classical ring-polymer model made of multiple beads (each bead refers to a classical system's configuration) with harmonic couplings between adjacent beads. For a finite number of P beads, the formal potential of the partition function $Q_P(\beta, N_e)$ in Eq. 12 is:

$$\begin{aligned}&\phi\left(\mathbf{R}^{(1)}, \cdots, \mathbf{R}^{(P)}, N_e\right) =\\ &\sum_{k=1}^{P}\left[\frac{1}{2}\omega_P^2\left(\mathbf{R}^{(k+1)}-\mathbf{R}^{(k)}\right)^T\underline{\boldsymbol{m}}\left(\mathbf{R}^{(k+1)}-\mathbf{R}^{(k)}\right)+\frac{1}{P}E\left(\mathbf{R}^{(k)}, N_e\right)\right]\Big|_{\mathbf{R}^{(1)}=\mathbf{R}^{(P+1)}}\end{aligned} \tag{13}$$

which is called the *effective potential*.

We define the centroid of multiple beads as $\mathbf{R}$, and usually, the RC of a quantum system is a function with respect to the centroid of multiple beads $q=f(\mathbf{R})$. The coordinate transformation to decouple the centroid has the form:

$$\begin{aligned}\mathbf{R} &= \frac{1}{P}\sum_{k=1}^{P}\mathbf{R}^{(k)}\\ \mathbf{R}_\Delta^{(k)} &= \mathbf{R}^{(k+1)}-\mathbf{R}^{(k)},\ k=1,\ \ldots,\ P-1\end{aligned} \tag{14}$$

In this situation, the probability density of $q=s$ is transformed into

$$\begin{aligned}P_P(s) &= \frac{\Lambda_P}{Q_P(\beta, N_e)}\int d\mathbf{R}^{(1)}\ldots d\mathbf{R}^{(P)}\exp\left[-\beta\phi\left(\mathbf{R}^{(1)}, \ldots, \mathbf{R}^{(P)}, N_e\right)\right]\delta(q-s)\\ &= \frac{\Lambda_P}{Q_P(\beta, N_e)}\int dq d\mathbf{q}_{\text{trans}} d\mathbf{q}_{\text{primit}} d\mathbf{R}_\Delta^{(1)}\ldots d\mathbf{R}_\Delta^{(P-1)}\delta(q-s)\mathcal{J}(q, \mathbf{q}_{\text{trans}})\\ &\quad\times\exp\left[-\beta\widetilde{\phi}\left(q, \mathbf{q}_{\text{trans}}, \mathbf{q}_{\text{primit}}, \mathbf{R}_\Delta^{(1)}, \ldots, \mathbf{R}_\Delta^{(P-1)}, N_e\right)\right]\\ &= \frac{\Lambda_P}{Q_P(\beta, N_e)}\int d\mathbf{q}_{\text{trans}}\mathcal{J}(s, \mathbf{q}_{\text{trans}})\int d\mathbf{q}_{\text{primit}}\int d\mathbf{R}_\Delta^{(1)}\ldots d\mathbf{R}_\Delta^{(P-1)}\\ &\quad\times\exp\left[-\beta\widetilde{\phi}\left(s, \mathbf{q}_{\text{trans}}, \mathbf{q}_{\text{primit}}, \mathbf{R}_\Delta^{(1)}, \ldots, \mathbf{R}_\Delta^{(P-1)}, N_e\right)\right]\end{aligned} \tag{15}$$

where $\{\mathbf{R}_\Delta^{(k)}\}_{k=1}^{P-1}$ are sampled via the staging transformation MC scheme[46,47] with $\mathbf{q}_{\text{trans}}$ and $\mathbf{q}_{\text{primit}}$ fixed. The evolution of $\mathbf{q}_{\text{trans}}$ and $\mathbf{q}_{\text{primit}}$ has been discussed in the above section. We further note that the force of the centroid under the *effective potential* is just the average force of all beads at their specific configurations.

Details of the mean force estimator

The free energy (potential of mean force) along a defined RC is a function of the probability density $P(s)$

$$F(s) = -\frac{1}{\beta}\ln P(s) \tag{16}$$

The free energy change between RC values s_1, s_2 can be computed by integrating the mean force along the RC range $[s_1, s_2]$

$$F(s_2)-F(s_1) = \int_{s_1}^{s_2}\frac{dF}{ds}ds = \int_{s_1}^{s_2}\left\langle\left(\frac{dF}{ds}\right)_{\text{estm}}\right\rangle_s^{\text{cond}}ds \tag{17}$$

where $\langle\cdot\rangle_s^{\text{cond}}$ represents the conditional ensemble average with the constraint $q=s$. According to the TI method, the general form of the estimator for the mean force is

$$\left(\frac{dF}{ds}\right)_{\text{estm}} = \frac{\partial\widetilde{E}}{\partial q}-k_B T\frac{\partial}{\partial q}\ln\mathcal{J}(\vec{\boldsymbol{q}}) \tag{18}$$

We consider two types of RCs in this study, and the specific formula of the estimator for them can be derived easily by the chain rule.

a. For $q = |\mathbf{R}_R - \mathbf{R}_L|$, the RC is defined as the distance between two particles labeled by L and R, and $\mathbf{R}_L$ and $\mathbf{R}_R$ are their positions. In this situation, the estimator is

$$\left(\frac{dF}{ds}\right)_{estm} = \frac{(\mathbf{f}_L - \mathbf{f}_R)(\mathbf{R}_R - \mathbf{R}_L) - 4k_BT}{2|\mathbf{R}_R - \mathbf{R}_L|} \quad (19)$$

b. For $q = |\mathbf{R}_R - \mathbf{R}_M| - |\mathbf{R}_M - \mathbf{R}_L|$, the RC is defined as the difference of the distance between two particles labeled by L and M and the distance between two particles labeled by M and R, and $\mathbf{R}_L$, $\mathbf{R}_M$, $\mathbf{R}_R$ are their positions. In this situation, the estimator is

$$\left(\frac{dF}{ds}\right)_{estm} = \frac{1}{2}\left[\frac{\mathbf{f}_L(\mathbf{R}_L - \mathbf{R}_M) + 2k_BT}{|\mathbf{R}_L - \mathbf{R}_M|} - \frac{\mathbf{f}_R(\mathbf{R}_R - \mathbf{R}_M) + 2k_BT}{|\mathbf{R}_R - \mathbf{R}_M|}\right] \quad (20)$$

where $\mathbf{f}_i$ is used to represent the force on the corresponding particle in the above two formulas.

Details of constrained PIHMC under GC sampling

We apply the constrained GC-(PI)HMC method on our modeled interface system at room temperature $T = 300$ K. The number of beads used in our PI calculations is 16 when we consider the NQEs of PCET steps[21,60]. Tests for the NQEs calculations in terms of beads number convergence and temperature effect can be found in Supplementary Note 7. In order to obtain more reliable statistical results, we perform 15 times independent 300,000-step sampling trajectories at different RC values for the Volmer reaction, each time with a different initial structure. For the Heyrovsky reaction, due to its better performance in the mean force convergence compared to the Volmer case, we perform 10 times independent mean force samplings for each RC case (also consisting of 300,000 (PI)HMC steps for every sampling trajectory). Specifically, for the sensitive RC range ($q_{Heyrovsky}$ from 0.85 to 0.95 Å) corresponding to the relative sharp transition of an H_2 molecule formation, we run each sampling trajectory for 1,000,000 steps to ensure the reliability of the ensemble average results.

Training process of our DP-N_e MLP

The MLP construction is conducted by the automatic configuration-exploration workflow DP-GEN[78] in this work. Concurrent learning processes in the DP-GEN contain a series of iterations, each of which is composed of three steps: training the neural network that describes force field models, exploring the configurational space (i.e., the extended [$\mathbf{R}$,N_e] space in our work), and labeling the newly added candidate configurations by first-principles calculations, which are selected based on evaluation of the current machine learning model's accuracy. Our DP-N_e model is generated according to the workflow displayed in Fig. 1b. We incorporate the total number of electrons N_e directly into the input layer of the neural network and use the software DeepMD-kit[79–83] to train the DP-N_e MLP. All exploration trajectories are performed under the GC ensemble distribution using our GC-HMC methods. More details about the DP-GEN iterations can be found in Supplementary Note 3.

Miscellaneous technical details in our sampling calculations

We implement several constraints on atomic coordinates to ensure reasonable configurational sampling in our GC-(PI)HMC simulations. We place a rigid wall ~1.1 Å below the compensating charge plate to prevent water molecules from diffusing to the vacuum region. As we only allow the transferring proton (originally in H^+_{sol} form) to move from IS to FS along our constrained HMC samplings in PCET free energy calculations, we have to make sure that H* atoms (except for the H* involved in the Heyrovsky step) at the Pt surface would not migrate to water layers. We thus introduce another rigid barrier, specifically for the adsorbed H* atoms, to prevent them from going upwards into the explicit H_2O molecule region. In addition, we place one more rigid wall, only for the solvation H_2O molecules, to avoid water adsorption at Pt sites which may disturb our free energy calculations of PCET reactions.

In our GC-PIHMC sampling simulations, trial moves for different types of degrees of freedom are selected based on a preset ratio. We set the probabilities of making trial moves for the internal degrees of freedom within the quantized beads' configurations in PIMC ($\mathbf{R}_\Delta^{(k)}$), centroid atomic coordinates ($\mathbf{R}$) and total number of electrons (N_e) as 0.32, 0.28, and 0.40, which corresponds to $a_1 = 0.32$ and $a_2 = 0.60$ mentioned in Fig. 1a.

Data availability

The result data from all the simulations in this study are provided within the paper or in the Supplementary Information file. Atomic coordinates of the optimized computational models and structure examples of the HMC sampling trajectories are provided in Supplementary Data 1. Source data are provided in this paper.

Code availability

The constrained GC-PIHMC code developed in this work is available at our group's GitHub page (https://github.com/sxu39/GC-Constrained-PIHMC) and on Code Ocean (https://doi.org/10.24433/CO.1818715.v2)[84].

References

1. Yusuf, B. A. et al. Recent advances in understanding and design of efficient hydrogen evolution electrocatalysts for water splitting: A comprehensive review. *Adv. Colloid Interface Sci.* **311**, 102811 (2023).
2. Zhao, Y. et al. Oxygen evolution/reduction reaction catalysts: From in situ monitoring and reaction mechanisms to rational design. *Chem. Rev.* **123**, 6257–6358 (2023).
3. Xu, S. & Carter, E. A. Theoretical insights into heterogeneous (Photo) electrochemical CO_2 reduction. *Chem. Rev.* **119**, 6631–6669 (2019).
4. Nørskov, J. K. et al. Origin of the overpotential for oxygen reduction at a fuel-cell cathode. *J. Phys. Chem. B* **108**, 17886–17892 (2004).
5. Chan, K. & Nørskov, J. K. Electrochemical barriers made simple. *J. Phys. Chem. Lett.* **6**, 2663–2668 (2015).
6. Chan, K. & Nørskov, J. K. Potential dependence of electrochemical barriers from ab initio calculations. *J. Phys. Chem. Lett.* **7**, 1686–1690 (2016).
7. Carter, E. A., Ciccotti, G., Hynes, J. T. & Kapral, R. Constrained reaction coordinate dynamics for the simulation of rare events. *Chem. Phys. Lett.* **156**, 472–477 (1989).
8. Sprik, M. & Ciccotti, G. Free energy from constrained molecular dynamics. *J. Chem. Phys.* **109**, 7737–7744 (1998).
9. Cheng, T., Xiao, H. & Goddard, W. A. Full atomistic reaction mechanism with kinetics for CO reduction on Cu(100) from ab initio molecular dynamics free-energy calculations at 298 K. *Proc. Natl. Acad. Sci. USA* **114**, 1795–1800 (2017).
10. Cao, H. et al. Engineering single-atom electrocatalysts for enhancing kinetics of acidic volmer reaction. *J. Am. Chem. Soc.* **145**, 13038–13047 (2023).
11. Cao, H., Zhang, Z., Chen, J.-W. & Wang, Y.-G. Potential-dependent free energy relationship in interpreting the electrochemical performance of CO2 reduction on single atom catalysts. *ACS Catal.* **12**, 6606–6617 (2022).
12. Kronberg, R. & Laasonen, K. Reconciling the experimental and computational hydrogen evolution activities of Pt(111) through DFT-based constrained MD simulations. *ACS Catal.* **11**, 8062–8078 (2021).
13. Sundararaman, R., Goddard, W. A. III & Arias, T. A. Grand canonical electronic density-functional theory: Algorithms and applications to electrochemistry. *J. Chem. Phys* **146**, 114104 (2017).

14. Chen, X. et al. Atomistic learning in the electronically grand-canonical ensemble. *Npj Comput. Mater.* **9**, 1–9 (2023).
15. Zhao, X. & Liu, Y. Origin of selective production of hydrogen peroxide by electrochemical oxygen reduction. *J. Am. Chem. Soc.* **143**, 9423–9428 (2021).
16. Bai, X. et al. Dynamic stability of copper single-atom catalysts under working conditions. *J. Am. Chem. Soc.* **144**, 17140–17148 (2022).
17. Xia, Z. & Xiao, H. Grand canonical ensemble modeling of electrochemical interfaces made simple. *J. Chem. Theory Comput.* **19**, 5168–5175 (2023).
18. Melander, M. M., Wu, T., Weckman, T. & Honkala, K. Constant inner potential DFT for modelling electrochemical systems under constant potential and bias. *npj Comput Mater* **10**, 1–11 (2024).
19. Ceriotti, M. et al. Nuclear quantum effects in water and aqueous systems: Experiment, theory, and Current challenges. *Chem. Rev.* **116**, 7529–7550 (2016).
20. Ganeshan, K. et al. Importance of nuclear quantum effects on aqueous electrolyte transport under confinement in Ti3C2 MXenes. *J. Chem. Theory Comput.* **18**, 6920–6931 (2022).
21. Tuckerman, M. E. & Marx, D. Heavy-atom skeleton quantization and proton tunneling in "Intermediate-Barrier" hydrogen bonds. *Phys. Rev. Lett.* **86**, 4946–4949 (2001).
22. Markland, T. E. & Ceriotti, M. Nuclear quantum effects enter the mainstream. *Nat. Rev. Chem.* **2**, 0109 (2018).
23. Zhang, Q., Wahnström, G., Björketun, M. E., Gao, S. & Wang, E. Path integral treatment of proton transport processes in BaZrO 3. *Phys. Rev. Lett.* **101**, 215902 (2008).
24. Warburton, R. E., Soudackov, A. V. & Hammes-Schiffer, S. Theoretical modeling of electrochemical proton-coupled electron transfer. *Chem. Rev.* **122**, 10599–10650 (2022).
25. Soudackov, A. & Hammes-Schiffer, S. Derivation of rate expressions for nonadiabatic proton-coupled electron transfer reactions in solution. *J. Chem. Phys* **113**, 2385–2396 (2000).
26. Goldsmith, Z. K., Lam, Y. C., Soudackov, A. V. & Hammes-Schiffer, S. Proton discharge on a gold electrode from triethylammonium in acetonitrile: Theoretical modeling of potential-dependent kinetic isotope effects. *J. Am. Chem. Soc.* **141**, 1084–1090 (2019).
27. Melander, M. M. Grand canonical rate theory for electrochemical and electrocatalytic systems I: General formulation and proton-coupled electron transfer reactions. *J. Electrochem. Soc.* **167**, 116518 (2020).
28. Feynman, R. P. Space-tme approach to non-relativistic quantum mechanics. *Rev. Mod. Phys.* **20**, 367–387 (1948).
29. Feynman, R. P., Hibbs, A. R. & Styer, D. F. *Quantum Mechanics and Path Integrals*. (Courier Corporation, 2010).
30. Zhang, L., Han, J., Wang, H., Car, R. & E, W. Deep potential molecular dynamics: A scalable model with the accuracy of quantum mechanics. *Phys. Rev. Lett.* **120**, 143001 (2018).
31. Yang, B., Ding, W., Zhang, H. & Zhang, S. Recent progress in electrochemical synthesis of ammonia from nitrogen: strategies to improve the catalytic activity and selectivity. *Energy Environ. Sci.* **14**, 672–687 (2021).
32. Kronberg, R., Lappalainen, H. & Laasonen, K. Revisiting the Volmer–Heyrovský mechanism of hydrogen evolution on a nitrogen doped carbon nanotube: constrained molecular dynamics versus the nudged elastic band method. *Phys. Chem. Chem. Phys.* **22**, 10536–10549 (2020).
33. Kastlunger, G., Lindgren, P. & Peterson, A. A. Controlled-potential simulation of elementary electrochemical reactions: Proton discharge on metal surfaces. *J. Phys. Chem. C* **122**, 12771–12781 (2018).
34. Skúlason, E. et al. Density functional theory calculations for the hydrogen evolution reaction in an electrochemical double layer on the Pt(111) electrode. *Phys. Chem. Chem. Phys.* **9**, 3241–3250 (2007).
35. Skúlason, E. et al. Modeling the electrochemical hydrogen oxidation and evolution reactions on the basis of density functional theory calculations. *J. Phys. Chem. C* **114**, 18182–18197 (2010).
36. Nørskov, J. K., Abild-Pedersen, F., Studt, F. & Bligaard, T. Density functional theory in surface chemistry and catalysis. *Proc. Natl. Acad. Sci. USA* **108**, 937–943 (2011).
37. Marković, N. M., Grgur, B. N. & Ross, P. N. Temperature-dependent hydrogen electrochemistry on platinum low-index single-crystal surfaces in acid solutions. *J. Phys. Chem. B* **101**, 5405–5413 (1997).
38. He, Z.-D., Wei, J., Chen, Y.-X., Santos, E. & Schmickler, W. Hydrogen evolution at Pt(111) – activation energy, frequency factor and hydrogen repulsion. *Electrochim. Acta* **255**, 391–395 (2017).
39. Metropolis, N., Rosenbluth, A. W., Rosenbluth, M. N., Teller, A. H. & Teller, E. Equation of state calculations by fast computing machines. *J. Chem. Phys.* **21**, 1087–1092 (1953).
40. Tuckerman, M. E. *Statistical Mechanics: Theory and Molecular Simulation*. (Oxford University Press, Oxford; New York, 2010).
41. Allen, M. P. & Tildesley, D. J. *Computer Simulation of Liquids (2nd Edn)*. (2017).
42. Duane, S., Kennedy, A. D., Pendleton, B. J. & Roweth, D. Hybrid Monte Carlo. *Phys. Lett. B* **195**, 216–222 (1987).
43. Mehlig, B., Heermann, D. W. & Forrest, B. M. Hybrid Monte Carlo method for condensed-matter systems. *Phys. Rev. B* **45**, 679–685 (1992).
44. Kirkwood, J. G. Statistical mechanics of fluid mixtures. *J. Chem. Phys.* **3**, 300–313 (1935).
45. Jin, B., Hu, T., Yu, K. & Xu, S. Constrained hybrid Monte Carlo sampling made simple for chemical reaction simulations. *J. Chem. Theory Comput.* **19**, 7343–7357 (2023).
46. Tuckerman, M. & Berne, B. J. Vibrational relaxation in simple fluids: Comparison of theory and simulation. *J. Chem. Phys.* **98**, 7301–7318 (1993).
47. Pollock, E. L. & Ceperley, D. M. Simulation of quantum many-body systems by path-integral methods. *Phys. Rev. B* **30**, 2555–2568 (1984).
48. Bonnet, N., Morishita, T., Sugino, O. & Otani, M. First-principles molecular dynamics at a constant electrode potential. *Phys. Rev. Lett.* **109**, 266101 (2012).
49. Ikeshoji, T., Uchida, T., Otani, M. & Osawa, M. First-principles molecular dynamics simulation for electrochemical hydrogen production by 4,4′-bipyridine molecular catalyst on silver electrode. *J. Electroanal. Chem.* **800**, 13–18 (2017).
50. Ikeshoji, T. & Otani, M. Toward full simulation of the electrochemical oxygen reduction reaction on Pt using first-principles and kinetic calculations. *Phys. Chem. Chem. Phys.* **19**, 4447–4453 (2017).
51. Levell, Z. et al. Emerging atomistic modeling methods for heterogeneous electrocatalysis. *Chem. Rev.* **124**, 8620–8656 (2024).
52. Conway, B. E. & Tilak, B. V. Interfacial processes involving electrocatalytic evolution and oxidation of H2, and the role of chemisorbed H. *Electrochim. Acta* **47**, 3571–3594 (2002).
53. Lindgren, P., Kastlunger, G. & Peterson, A. A. A challenge to the $G \sim 0$ interpretation of hydrogen evolution. *ACS Catal.* **10**, 121–128 (2020).
54. Olsen, R. A., Kroes, G. J. & Baerends, E. J. Atomic and molecular hydrogen interacting with Pt(111). *J. Chem. Phys.* **111**, 11155–11163 (1999).
55. Ford, D. C., Xu, Y. & Mavrikakis, M. Atomic and molecular adsorption on Pt(1 1 1). *Surf. Sci.* **587**, 159–174 (2005).
56. Karimadom, B. R. et al. Hydrogen adsorption on various transition metal (111) surfaces in water: a DFT forecast. *Phys. Chem. Chem. Phys.* **26**, 7647–7657 (2024).
57. Kronberg, R. & Laasonen, K. Coupling surface coverage and electrostatic effects on the interfacial adlayer–water structure of hydrogenated single-crystal platinum electrodes. *J. Phys. Chem. C* **124**, 13706–13714 (2020).
58. Nanbu, N., Kitamura, F., Ohsaka, T. & Tokuda, K. Adsorption of atomic hydrogen on a polycrystalline Pt electrode surface studied by FT-IRAS: the influence of adsorbed carbon monoxide on the spectral feature. *J. Electroanal. Chem.* **485**, 128–134 (2000).

59. Bi, C. & Yang, Y. Atomic resonant tunneling in the surface diffusion of H atoms on Pt(111). *J. Phys. Chem. C* **125**, 464–480 (2021).
60. Yan, L., Yamamoto, Y., Shiga, M. & Sugino, O. Nuclear quantum effect for hydrogen adsorption on Pt(111). *Phys. Rev. B* **101**, 165414 (2020).
61. Brumme, T., Calandra, M. & Mauri, F. Electrochemical doping of few-layer ZrNCl from first principles: Electronic and structural properties in field-effect configuration. *Phys. Rev. B* **89**, 245406 (2014).
62. Lozovoi, A. Y., Alavi, A., Kohanoff, J. & Lynden-Bell, R. M. Ab initio simulation of charged slabs at constant chemical potential. *J. Chem. Phys* **115**, 1661–1669 (2001).
63. Chen, M., Guo, G.-C. & He, L. Systematically improvable optimized atomic basis sets for ab initio calculations. *J. Phys. Condens. Matter* **22**, 445501 (2010).
64. Li, P. et al. Large-scale ab initio simulations based on systematically improvable atomic basis. *Comput. Mater. Sci.* **112**, 503–517 (2016).
65. Giannozzi, P. et al. QUANTUM ESPRESSO: a modular and open-source software project for quantum simulations of materials. *J. Phys. Condens. Matter* **21**, 395502 (2009).
66. Giannozzi, P. et al. Advanced capabilities for materials modelling with Quantum ESPRESSO. *J. Phys. Condens. Matter* **29**, 465901 (2017).
67. Bocus, M. et al. Nuclear quantum effects on zeolite proton hopping kinetics explored with machine learning potentials and path integral molecular dynamics. *Nat. Commun.* **14**, 1008 (2023).
68. Perdew, J. P., Burke, K. & Ernzerhof, M. Generalized gradient approximation made simple. *Phys. Rev. Lett.* **77**, 3865–3868 (1996).
69. Bengtsson, L. Dipole correction for surface supercell calculations. *Phys. Rev. B* **59**, 12301–12304 (1999).
70. Grimme, S., Antony, J., Ehrlich, S. & Krieg, H. A consistent and accurate ab initio parametrization of density functional dispersion correction (DFT-D) for the 94 elements H-Pu. *J. Chem. Phys.* **132**, 154104 (2010).
71. Trasatti, S. The absolute electrode potential: an explanatory note (Recommendations 1986). *Pure Appl. Chem.* **58**, 955–966 (1986).
72. Fawcett, W. R. The ionic work function and its role in estimating absolute electrode potentials. *Langmuir* **24**, 9868–9875 (2008).
73. Cao, H., Lv, X., Qian, S., Li, J. & Wang, Y.-G. Constant potential thermodynamic integration for obtaining the free energy profile of electrochemical reaction. *J. Phys. Chem. Lett.* **15**, 1314–1320 (2024).
74. Li, Y., Suleimanov, Y. V., Li, J., Green, W. H. & Guo, H. Rate coefficients and kinetic isotope effects of the X + CH4 → CH3 + HX (X = H, D, Mu) reactions from ring polymer molecular dynamics. *J. Chem. Phys.* **138**, 094307 (2013).
75. Suleimanov, Yu. V., Allen, J. W. & Green, W. H. RPMDrate: Bimolecular chemical reaction rates from ring polymer molecular dynamics. *Comput. Phys. Commun.* **184**, 833–840 (2013).
76. Zhang, L., Zuo, J., Suleimanov, Y. V. & Guo, H. Ring polymer molecular dynamics approach to quantum dissociative chemisorption rates. *J. Phys. Chem. Lett.* **14**, 7118–7125 (2023).
77. Exner, K. S., Sohrabnejad-Eskan, I. & Over, H. A universal approach to determine the free energy diagram of an electrocatalytic reaction. *ACS Catal* **8**, 1864–1879 (2018).
78. Zhang, Y. et al. DP-GEN: A concurrent learning platform for the generation of reliable deep learning based potential energy models. *Comput. Phys. Commun.* **253**, 107206 (2020).
79. Han, J., Zhang, L., Car, R. & E, W. Deep Potential: a general representation of a many-body potential energy surface. *Commun. Comput. Phys.* **23**, 629–639 (2018).
80. Zhang, L., Lin, D.-Y., Wang, H., Car, R. & E, W. Active learning of uniformly accurate interatomic potentials for materials simulation. *Phys. Rev. Mater.* **3**, 023804 (2019).
81. Lu, D. et al. 86 PFLOPS Deep potential molecular dynamics simulation of 100 million atoms with ab initio accuracy. *Comput. Phys. Commun.* **259**, 107624 (2021).
82. Lu, D. et al. DP Compress: A model compression scheme for generating efficient deep potential models. *J. Chem. Theory Comput.* **18**, 5559–5567 (2022).
83. Zeng, J. et al. DeePMD-kit v2: A software package for deep potential models. *J. Chem. Phys.* **159**, 054801 (2023).
84. Jin, B., Sun, M., Yang, X. & Xu, S. Probing Nuclear Quantum Effects in Electrocatalysis via a Machine-Learning Enhanced Grand Canonical Constant Potential Approach. https://doi.org/10.24433/CO.1818715.v2 (2025).

Acknowledgements

The authors gratefully acknowledge funding support from the National Natural Science Foundation of China (grant no. 92470114, no. 52273223), Ministry of Science and Technology of the People's Republic of China (grant no. 2021YFB3800303), DP Technology Corporation (grant no. 2021110016001141), School of Materials Science and Engineering at Peking University, and the AI for Science Institute, Beijing (AISI). The computing resource of this work was provided by the Bohrium Cloud Platform (https://bohrium.dp.tech), which was supported by DP Technology.

Author contributions

M.S. performed calculations, post-processed the data, and analyzed the results. B.J. implemented the method and developed the initial framework. X.Y. performed calculations and assisted in the data analysis. S.X. conceived and designed the scope of the project. M.S. and S.X. drafted the manuscript, while all other authors provided input on writing. M.S. and S.X. reviewed the manuscript.

Competing interests

The authors declare no competing interests.

Additional information

Supplementary information The online version contains supplementary material available at https://doi.org/10.1038/s41467-025-58871-7.

Correspondence and requests for materials should be addressed to Shenzhen Xu.

Peer review information *Nature Communications* thanks David Hernandez Castillo, and the other anonymous reviewer(s) for their contribution to the peer review of this work. A peer review file is available.